Atomistic insights into the effects of doping and vacancy clustering on Li-ion conduction in the Li_3OCl anti-perovskite solid electrolyte

Matt Clarke,[a] James A Dawson,[b] Tim Mays[c] and M. Saiful Islam[a‡]

[a] *Department of Chemistry, University of Bath, Bath, BA2 7AY, UK. E-mail: M.J.Clarke@bath.ac.uk, M.S.Islam@bath.ac.uk*
[b] *Chemistry – School of Natural and Environmental Science, Newcastle University, NE1 7RU, UK.*
[c] *Department of Chemical Engineering, University of Bath, Bath, BA2 7AY, UK.*

Abstract

Solid-state batteries are currently attracting increased attention because of their potential for significant improvements in energy density and safety as compared to liquid electrolyte-based batteries. Lithium-rich anti-perovskites, such as Li_3OCl, are of particular interest, but the effects of doping on lithium mobility are not fully understood at the atomic level. Here we investigate the impact of divalent cation (Mg^{2+}, Ca^{2+}, Sr^{2+}, and Ba^{2+}) and F^- doping on the ion conduction properties of Li_3OCl, using both defect simulation and molecular dynamics techniques. Our results show that the F-doped system has a low conductivity and high activation barriers. This is attributable to high binding energies, which leads to the formation of stable dopant-vacancy pairs, preventing long-range lithium-ion mobility. In contrast to the F-doped system, Mg dopants (shown to be the most favourable dopant on the Li^+ site) have lower binding energies to lithium vacancies, yielding higher lithium-ion conductivities and lower migration energies. Our results indicate a viable doping strategy to improve the electrochemical performance of anti-perovskite solid electrolytes.

1 Introduction

Solid electrolytes have attracted significant research in recent years, due to the safety, stability, and energy density benefits which solid-state batteries can provide over conventional liquid electrolyte systems.[1–15] In particular, solid electrolytes may enable the use of high voltage electrodes or lithium-metal anodes, which are incompatible with current liquid electrolytes.[3,4,16,17] However, despite the potential benefits of solid electrolytes, transport issues at the electrode interface and the reduced ionic conductivity versus their liquid counterparts have thus far prevented their wide-spread adoption.[3,6,7,18,19]

Li-rich anti-perovskites (Li_3OX with X = Cl or Br) are promising solid electrolyte candidates, with good cyclability, high stability, wide electrochemical windows, and negligible electronic conductivity.[20–25] The perovskite structure is also highly amenable to chemical substitution

and modification, allowing for the optimisation of ionic conductivity or stability.[20,26,27] Early work by Zhao and Daemen[20] reported migration barriers as low as 0.2–0.3 eV, and conductivities of 1.94×10^{-3} Scm^{-1} at room temperature, which compares favourably with mature systems such as the LLZO garnet[28] at 2.06×10^{-3} Scm^{-1}. However, subsequent studies on Li_3OCl have indicated higher migration barriers (~0.6 eV) and lower conductivities.[29–34] A number of reasons for this discrepancy have been proposed, including the formation of hydroxide derivatives,[30,35–37], grain boundary effects[38–40] and inadvertent cation doping during synthesis.[34] Issues surrounding the hygroscopic nature of antiperovskites and stability at high voltages are potential barriers to practical applications.[1,41]

In attempts to enhance their performance, a range of chemical modifications have been studied, including the mixing of mobile ions, doping, and the incorporation of polyanionic species.[20,32,42–49] Braga *et al.*[43,44] demonstrated that divalent doping (M = Mg^{2+}, Ca^{2+}, or Ba^{2+}) increased the Li-ion conductivity of Li_3OCl by an order of magnitude. Mg^{2+} doping is of particular interest, as its small ionic radius limits lattice distortion, preventing glass formation at low temperatures.[45] Fluorine doping in the hydrated anti-perovskite $Li_2(OH)X$ (X = Cl or Br) has been demonstrated to enhance ionic conductivity by Li *et al.*[32], but has not been considered in the context of Li_3OCl.

Despite the recent interest in lithium-rich anti-perovskites, there is limited information on the fundamental atomistic factors that control their macroscopic dopant properties, which is valuable in facilitating targeted experimental work. An understanding of the interactions between mobile ions and dopant species over large time- and length-scales is key to overcoming known limiting factors, such as grain boundary resistance. Here we address this shortcoming by studying the impact of divalent cation (Mg^{2+}, Ca^{2+}, Sr^{2+}, and Ba^{2+}) and F^- doping on the Li-ion transport properties of Li_3OCl. In particular, we consider the modes of dopant incorporation and the possibility of defect clustering from dopant-vacancy interactions in order to develop an atomistic understanding of the factors that may affect long-range lithium-ion conduction.

2 Results and Discussion

2.1 Dopant reactions and Li-ion conductivity

The Li_3OCl anti-perovskite crystal structure consists of oxide ions at the typical B-site of an ABX_3 perovskite, coordinated to six Li^+ ions at the X-site, and the large Cl^- ion occupying the 12-coordinate A-site, as shown in Figure 1a. The simulated lattice parameter for bulk Li_3OCl is 3.921Å, with only a −0.36 % difference to the observed diffraction value of 3.907Å,[50] showing good reproduction of the experimental structure.

In terms of modes of dopant incorporation, cation dopants can substitute at the Li site, whereas anion dopants can sit at either O or Cl sites with the creation of charge compensating defects where necessary. This raises key questions in relation to the favoured substitution site, the type of compensating defect, and the influence (if any) of host ion size. Our simulation methods can probe these issues by generating quantitative estimates of the

relative energies of different modes of dopant incorporation (sometimes termed modes of solution). Although the prediction of the precise amount of dopant that can be incorporated is less straightforward, our results can provide a useful systematic guide to the site-selectivity for different dopant species and to trends in dopant solubility. Such an approach has been applied successfully to a variety of perovskite oxide ionic conductors.[51–53]

We have therefore examined a range of dopants in Li_3OCl including divalent cations (Mg, Ca, Sr, and Ba) on the Li site and F^- on the O site. In order to form lithium vacancies, the following solution modes are viable:

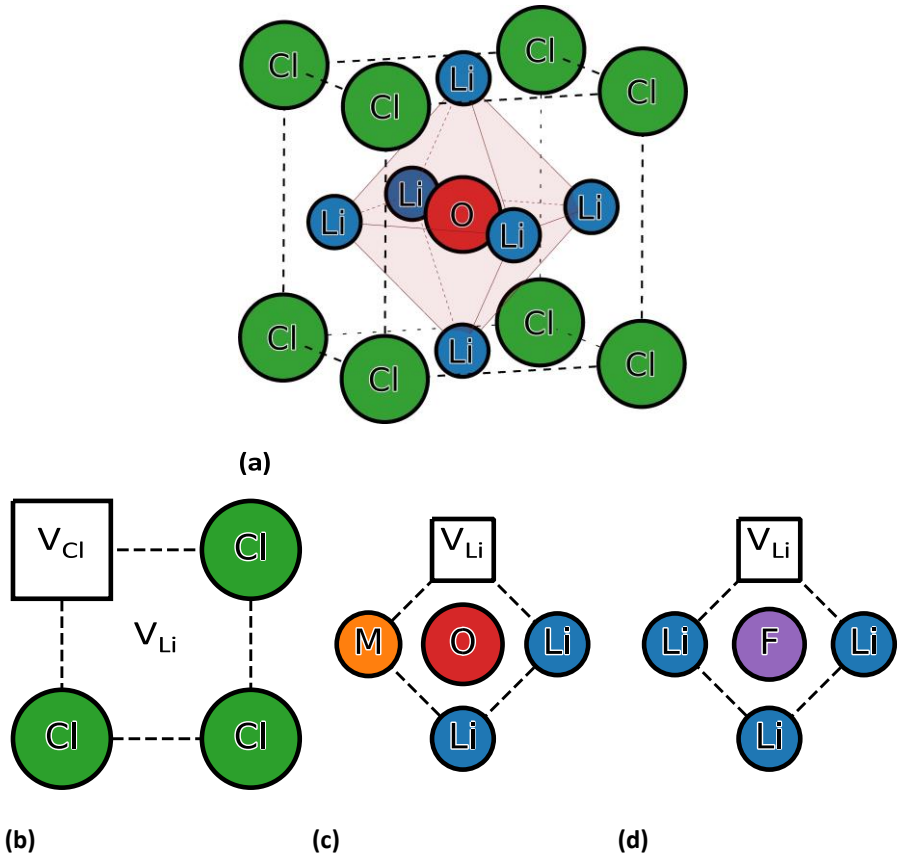

Figure 1 (a) Anti-perovskite crystal structure of Li_3OCl; and nearest-neighbour defect pair clusters for (b) LiCl Schottky defects, (c) M^{2+} doping, and (d) F^- doping in anti-perovskite Li_3OCl. Li^+ ions are shown in blue, O^{2-} in red, Cl^- in green, F^- in purple, and M^{2+} in orange.

Vacancies are indicated by black squares.

M^{2+} on Li^+ site charge compensated by V^0_{Li}

$$MCl_2 + 2Li^{\times}_{Li} \longrightarrow M^{\bullet}_{Li} + V'_{Li} + 2LiCl \qquad (1)$$

F^- on O^{2-} site charge compensated by V^0_{Li}

$$LiF + Li^{\times}_{Li} + O^{\times}_{O} \longrightarrow F^{\bullet}_{O} + V^{0}_{Li} + Li_2O \quad (2)$$

where in Kroger-Vink notation, $M^{\bullet}_{Li}$ and $F^{\bullet}_{O}$ signify M^{2+} and F^- dopant substitutional defects respectively, with V^0_{Li} signifying a Li^+ vacancy. However, the possibility of other favourable compensation mechanisms could prevent dopants from creating the desired lithium vacancies required for long-range diffusion:

M^{2+} on Li^+ site charge compensated by Cl^0_i

$$MCl_2 + Li^{\times}_{Li} \longrightarrow M^{\bullet}_{Li} + Cl^{0}_{i} + LiCl \quad (3)$$

F^- on Cl^- site

$$LiF + Cl^{\times}_{Cl} \longrightarrow F^{\times}_{Cl} + LiCl \quad (4)$$

where Cl^0_i indicates an Cl^- interstitial defect. The energies of these "solution" reactions can be evaluated combining appropriate defect energies from simulation methods and lattice energy values.

Calculated solution energies are presented in Figure 2 and three main features emerge. First, Mg^{2+} doping on the Li site is the most energetically favourable dopant, whereas larger ions are far less soluble; this indicates that Mg doping would show the highest solubility and be the most effective in creating mobile Li vacancies. These trends may be related to the similarity in ionic size between dopants and the substituted host ion, consistent with dopant substitution in ion-conducting perovskite oxides.[53-55]

Second, M^{2+} doping on Li^+ sites with charge-compensation via Cl^- interstitial defects is relatively unfavourable suggesting that such interstitial defects are highly unlikely in the close-packed anti-perovskite structure; indeed, anion interstitials have not been observed experimentally in the much-studied $BaMO_3$ and $LaMO_3$ perovskite ionic conductors.[54] We note that solution energies derived using dopant oxides as reference states are also presented Figure S2, which yielded similar trends to the dopant chlorides (Eq 1), but slightly higher solution energies for the favourable Mg dopant.

Third, for F-doping the isovalent mechanism (Eq 4) is more energetically favourable than the reaction involving lithium vacancy compensation. As vacant lithium sites are key to improving lithium-ion conductivity in Li_3OCl, there may be motivation to overcome this by non-stoichiometric synthesis routes should it significantly improve Li-ion conductivity.

In addition to divalent cations, we note that Al^{3+} was considered as a potential dopant at the Li site with both Li-vacancy and O-interstitial compensation. However, large calculated energies for both solution modes (8.89 eV for Eq 1 and 11.38 eV for Eq 3) indicate unfavourable incorporation. This result suggests that Al^{3+} doping may not be the main reason for the enhanced Li-ion conductivity observed in early studies on this material.[20,34]

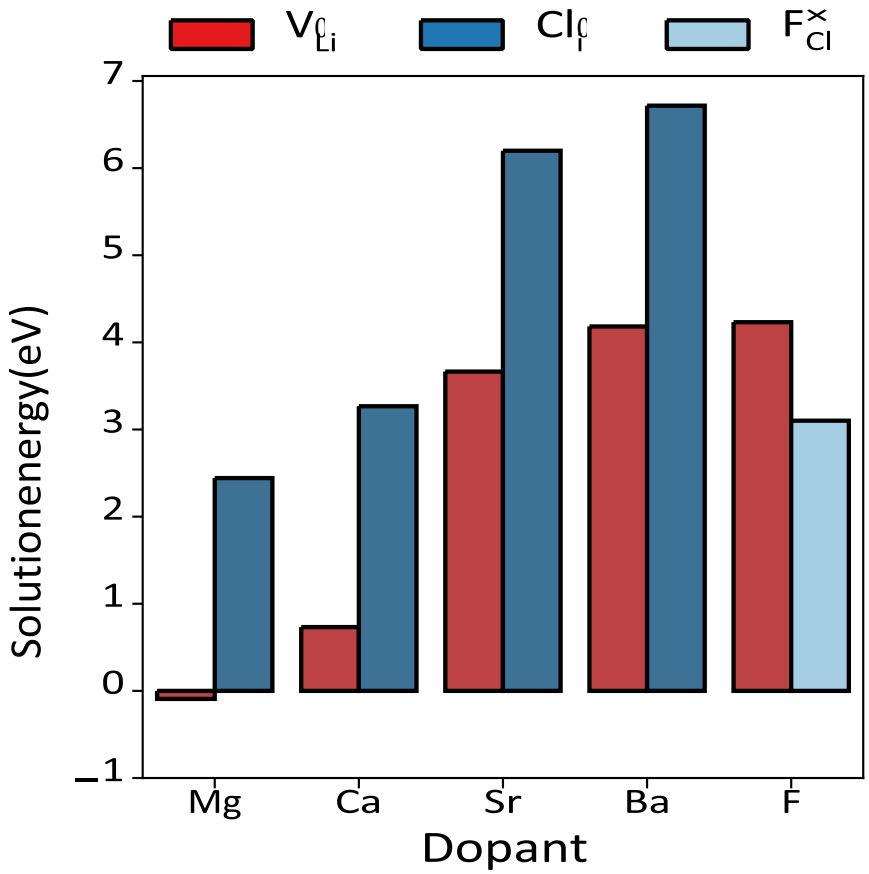

Figure 2 Dopant solution energies for M^{2+} doping and F^- doping in anti-perovskite Li_3OCl. Both V^0_{Li} (Eq 1) and Cl^0_i (Eq 3) are considered as charge compensation mechanisms for M^{2+} doping, whilst V^0_{Li} (Eq 2) compensated and isovalent $F^{\times}_{Cl}$ doping (Eq 4) are considered for F^- doping.

Turning now to ion transport, molecular dynamics (MD) simulation techniques allow us to investigate the Li-ion conduction properties as a function of charge-carrier concentration and temperature. We use large-scale MD calculations of both undoped and doped Li_3OCl at a range of lithium vacancy concentrations; we stress that our simulations and diffusion statistics using large supercells (>17,000 ions) and long time-scales (1ns) are orders of magnitude greater than that currently attainable by ab initio MD. Mg and F dopants are considered, as the most energetically favourable dopants. A low level of cation vacancies (via LiCl Schottky defects) are introduced in the undoped system to facilitate lithium mobility.

Figure 3 shows an Arrhenius plot of the temperature-dependant lithium-ion conductivity for each system. The undoped system shows conductivities of 3.0×10^{-3} Scm^{-1} at 500K, in good agreement with experimental impedance spectroscopy measurements ($\sim2.7\times10^{-3}$ Scm^{-1}).[20]

Mg-doping leads to a slight decrease in ionic conductivity, with activation barriers of 0.41 eV in good agreement with experimental studies (0.46 eV).[44] However, this is offset by the far higher Li-vacancy concentrations achievable by doping than occur in undoped Li_3OCl. The

conductivity of the F-doped systems are approximately two orders of magnitude lower than undoped Li_3OCl at 700 K, with significantly increased migration barriers in the F-doped system (0.89 eV), both of which are key properties for electrolyte performance. At lower temperatures, Li mobility is insufficient to accurately calculate activation barriers over the timescale studied, so these temperatures were excluded from the fitting.

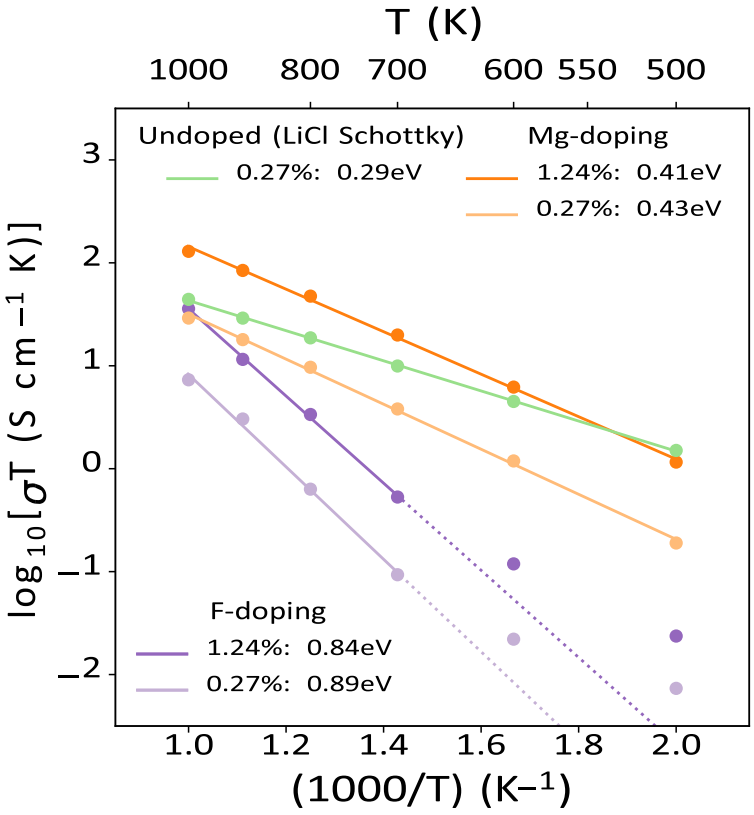

Figure 3 Temperature-dependent Li^+ conductivities (σT) and activation energies (E_a) for F and Mg doped Li_3OCl at two lithium vacancy concentrations compared to a low concentration in the undoped system. Solid lines indicate the data from which migration barriers were calculated. Dashed lines indicate extrapolated conductivities in the F-doped system, where Li mobility decreases significantly at lower temperatures.

2.2 Dopant–vacancy association in doped Li_3OCl

It is well established that charged point defects can associate to form localised clusters, which can have significant effects on transport behaviour.[54,56] An analysis of the ion dynamics and time-scale over which these defect clusters form on the atomic-scale has not yet been considered for doped Li_3OCl, and often detailed experimental characterisation of such defect clusters can be difficult. Our simulation methods can model the electrostatic, polarization

and elastic strain energies, which are the predominant terms in any local defect association process.

Energy minimisation calculations were performed to determine the binding energies of dopant–vacancy pairs in Li_3OCl. Figures 1b – 1d show the configurations of dopant– vacancy clusters for F^- and M^{2+} doping, along with the Li/Cl vacancy pair (LiCl Schottky) which facilitates lithium mobility in the undoped system.[57] At the dilute limit, binding energies can be calculated by:

$$E_{\text{bind}} = E_{\text{cluster}} - \sum_{i=1}^{N} E_{\text{dilute}}{}^{i} \quad (5)$$

where E_{bind} is the binding energy, E_{cluster} is the energy of the defect pair cluster, and E_{dilute} is the energy of an isolated component of the N defect cluster components at the dilute limit. At higher concentrations, all inequivalent configurations of a Li_3OCl supercell at a given size are relaxed, with a binding energy given by:

$$E_{\text{bind}} = E_{\text{cluster}} - \max(E_{\text{configs}}) \quad (6)$$

where E_{configs} is the energies of all unique configurations.

Figure 4 shows the calculated binding energies of dopant-vacancy pairs with three main features that can be identified. First, Mg^{2+} has the smallest vacancy binding energies for divalent cation doping. At the dilute limit, Li vacancies are loosely bound to Mg dopants, with only slightly higher binding energies than the undoped system. This indicates that dopant-vacancy interactions will not significantly reduce the lithium-ion mobility of Mg-doped Li_3OCl. The similarity between the ionic radii of Mg and Li (0.72 and 0.76 Å, respectively)[58] limits local lattice distortion. Larger degrees of local lattice distortion is known to result in increased elastic or polarisation effects, explaining the comparatively high binding energies calculated for larger M^{2+} dopant ions.

Second, the highest dopant-vacancy binding energies are found at the dilute limit, with binding energies decreasing for the 1.24% dopant concentration. This is attributed to dopant-vacancy-dopant interactions, with vacancies in a pair being attracted to other nearby dopants, offsetting the binding energy of the isolated cluster. Previous DFT studies on this system predict that M^{2+} doping in Li_3OCl forms dopant-vacancy pair clusters at low temperatures[44,45] but did not consider higher dopant concentrations or high temperatures.

Third, all other M^{2+} dopants and F^- doping on the O site show high binding energies (> 0.5 eV), which would significantly hinder lithium mobility in these materials, reducing their viability as solid electrolytes. The high binding energies for F doping on the O site likely arises due to the smaller Li-O interatomic distances (1.96Å) than the separations Li-Cl (2.77Å). These results suggest clustering of F dopant ions and Li vacancies (rather than a random distribution) as possible

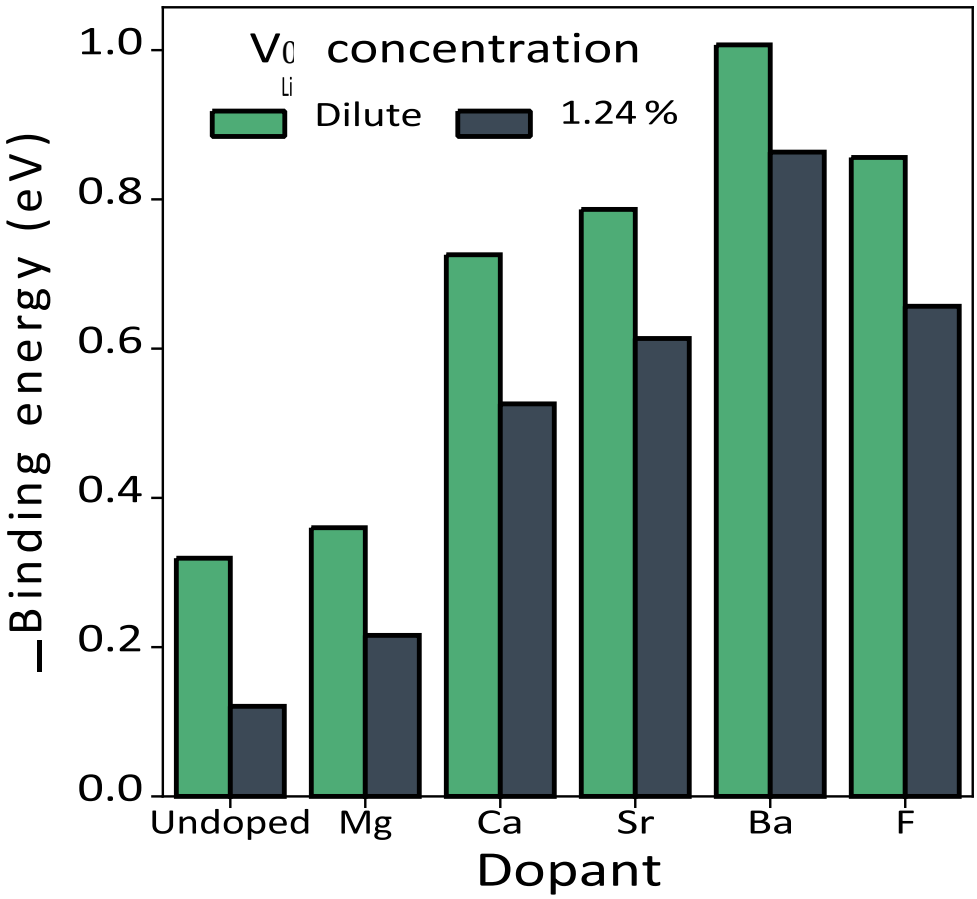

Figure 4 Defect binding energies for M^{2+} (Eq. 1) and F^- (Eq. 2) dopants in Li_3OCl for two lithium vacancy concentrations.

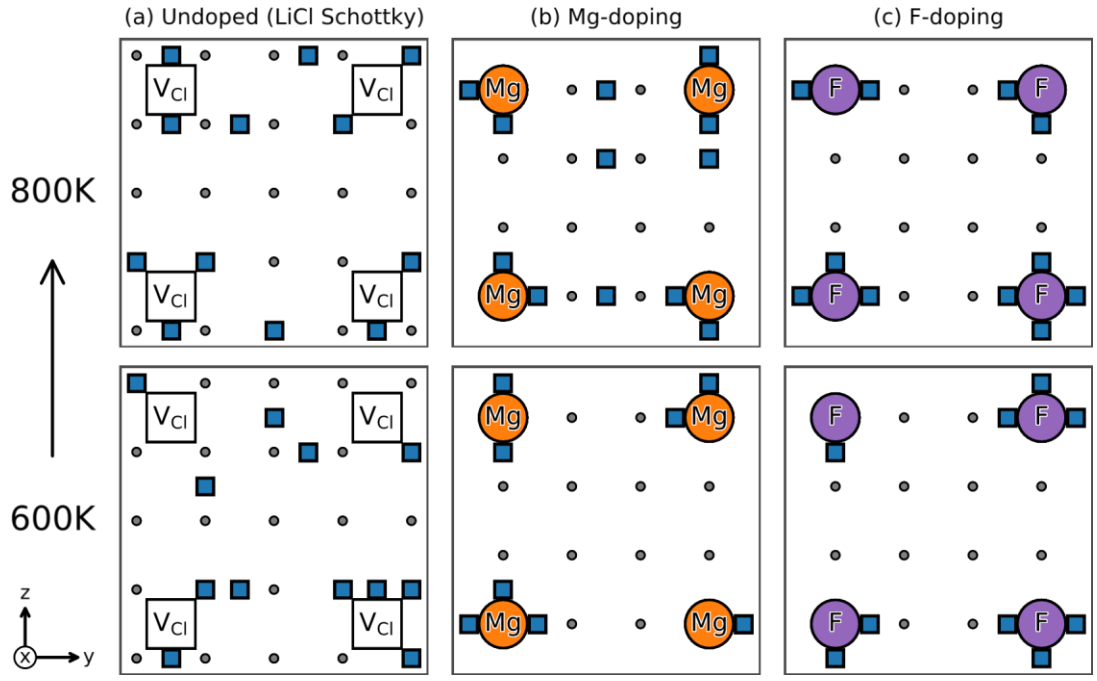

Figure 5 Flattened view along [100] (~60Å depth) to illustrate defect clustering effects from MD simulations at two temperatures, 600 K and 800 K (*t* = 150 ps). (a) undoped (b) Mg-doped (c) F-doped. 1.24 % of lithium sites are vacant, indicated by blue squares. Cl vacancies are shown with hollow squares, Mg dopants with orange circles, F dopants with purple circles, and O sites with small grey circles. Occupied Li and Cl sites have been omitted for clarity.

precursors to larger clusters or nano-domains, which we then examine using the MD simulation data.

Figure 5 shows the distribution of lithium vacancies in three different structures at two temperatures: undoped, Mg-doped, and F-doped systems. A high distribution of free vacancies indicates that the binding energies are small relative to the average kinetic energy of lithium ions at a given temperature, whilst dopant-vacancy clusters indicate that the binding energy is sufficient to inhibit long-range lithium-ion mobility. The presence of these dopant clusters within the short simulation timescale indicates that defect clustering is a favourable and rapid process.

In the undoped system, lithium vacancies are widely distributed at 600K, indicating that the binding energy is insufficient to significantly inhibit lithium mobility at this temperature. We note that LiCl Schottky defects are not expected to form at these concentrations, but are considered here to allow direct comparison. In contrast, the majority of lithium vacancies are adjacent to a dopant site in both the Mg- and F-doped systems at 600K. At 800K, lithium vacancies are found to more frequently dissociate from Mg dopant ions, whilst remaining bound to F sites. The significant differences in Li-ion conductivity found between systems can be rationalised by Li vacancy trapping effects preventing long-range lithium mobility in

systems with higher binding energies. One of the aims of this work is to encourage further structural study to probe such defect clustering at the local level.

3 Conclusions

An understanding of the mechanisms that both enhance and inhibit lithium-ion conductivity is vital if next-generation solid electrolytes are to be realised. In this study, we have gained quantitative and atomistic details on the modes of dopant incorporation, the dopant-vacancy binding energies, and the Li-ion transport properties of F- and Mg-doped Li_3OCl.

Three key conclusions can be drawn. First, the most favourable doping mechanism is Mg incorporation with Li vacancy compensation, which would facilitate Li-ion conductivity. Second, the increase in Li vacancy concentration and lower dopant-vacancy binding energy for Mg-doping provides a means of improving the electrochemical performance of Li_3OCl. Third, high binding energies between F-dopants and lithium vacancies lead to defect clustering and significantly higher Li-ion migration barriers, inhibiting long-range Li-ion migration in accord with the observed decrease in Li-ion conductivity in F-doped Li_3OCl. The lack of long-range Li-ion transport can be rationalised by considering the trapping of Li vacancies.

The tuning of vital solid electrolyte properties, such as Li-ion conductivity and electrochemical stability, via extrinsic doping is essential to achieve state-of-the-art solid-state batteries. The atomistic insights described in this work illustrate the importance of considering the binding between dopants and Li-ion charge-carriers, since it can potentially eclipse the anticipated benefit of having a high charge-carrier concentration.

4 Methods

Atomistic simulation methods based on effective interatomic potentials are widely used and have been described more thoroughly elsewhere.[54,56] Previous studies on solid electrolyte materials including undoped Li_3OCl have successfully applied these techniques to yield both structural and ion transport properties.[38,42,59–62] Such atomistic techniques have the advantage of examining defect and ionic conduction processes at much larger length- and time-scales than electronic structure methods.

Short-range ion interactions are modelled using Buckingham-type interatomic potentials, whilst long-range interactions are modelled using Coulombic terms. Energy minimisation calculations account for local polarisation effects via the shell model, allowing the displacement of ion shells from their cores subject to a harmonic potential.[63] Interatomic potential parameters are given in Supplementary Information (Tables S1 and S2). Defect energies at dilute concentrations are calculated using the Mott–Littleton approximation,[64] implemented in the General Utility Lattice Program (GULP).[65]

The LAMMPS[66] code was used for all molecular dynamics (MD) calculations. Long time-scale simulations of 10ns were performed with a time step of 1fs, with supercells containing around 17,000-20,000 ions, to ensure confidence in the calculated conductivities and activation barriers. Lithium vacancies are initially distributed randomly, whilst positive defects (Cl vacancy, Mg dopant, and F dopant) are distributed in a symmetric arrangement

to maximise their ion-ion spacing. Simulations were carried out over a temperature range of 500 to 1000K in intervals of 100K in the NPT ensemble using a Nosé-Hoover thermostat.[67] Conductivities were derived from the mean-squared displacement (MSD) of lithium ions and calculated using the Nernst–Einstein equation, with a Haven ratio of 1 as in previous studies.[31,38,42,59] The tracking of individual vacancies utilises Wigner–Seitz cell analysis, comparing doped and thermally distorted systems at a given time step to a pristine reference lattice.[68,69]

Acknowledgements

For jointly funding a PhD studentship, the authors thank the EPSRC Centre for Doctoral Training in Sustainable Chemical Technologies (EP/L016354/1) and CFH Docmail. The Faraday Institution (FIRG003) is gratefully acknowledged for MICHAEL supercomputer resources. We also thank the HEC Materials Chemistry Consortium (EP/R029431) for Archer supercomputer facilities. JAD also acknowledges Newcastle University for funding through a Newcastle Academic Track (NUAcT) Fellowship.

References

[1] D. Campanella, D. Belanger and A. Paolella, *Journal of Power Sources*, 2021, **482**, 228949.

[2] F. Zhu, M. S. Islam, L. Zhou, Z. Gu, T. Liu, X. Wang, J. Luo, C. W. Nan, Y. Mo and C. Ma, *Nature Communications*, 2020, **11**, 1–9.

[3] T. Famprikis, P. Canepa, J. A. Dawson, M. S. Islam and C. Masquelier, *Nature Materials*, 2019, **18**, 1278–1291.

[4] D. Lin, Y. Liu and Y. Cui, *Nature Nanotechnology*, 2017, **12**, 194–206.

[5] Y. Guo, H. Li and T. Zhai, *Advanced Materials*, 2017, **29**, 1–25.

[6] Z. Gao, H. Sun, L. Fu, F. Ye, Y. Zhang, W. Luo and Y. Huang, *Advanced Materials*, 2018, **30**, 1–27.

[7] K. Kerman, A. Luntz, V. Viswanathan, Y.-M. Chiang and Z. Chen, *Journal of The Electrochemical Society*, 2017, **164**, A1731–A1744.

[8] J.-J. Kim, K. Yoon, I. Park and K. Kang, *Small Methods*, 2017, **1**, 1700219.

[9] A. Manthiram, X. Yu and S. Wang, *Nature Reviews Materials*, 2017, **2**, 1–16.

[10] R. Chen, W. Qu, X. Guo, L. Li and F. Wu, *Materials Horizons*, 2016, **3**, 487–516.

[11] J. C. Bachman, S. Muy, A. Grimaud, H. H. Chang, N. Pour, S. F. Lux, O. Paschos, F. Maglia, S. Lupart, P. Lamp, L. Giordano and Y. Shao-Horn, *Chemical Reviews*, 2016, **116**, 140–162.

[12] W. D. Richards, L. J. Miara, Y. Wang, J. C. Kim and G. Ceder, *Chemistry of Materials*, 2016, **28**, 266–273.

[13] M. D. Tikekar, S. Choudhury, Z. Tu and L. A. Archer, *Nature Energy*, 2016, **1**, 1–7.

[14] J. Li, C. Ma, M. Chi, C. Liang and N. J. Dudney, *Advanced Energy Materials*, 2015, **5**, 1–6.

[15] Y. Wang, W. D. Richards, S. P. Ong, L. J. Miara, J. C. Kim, Y. Mo and G. Ceder, *Nature Materials*, 2015, **14**, 1026–1031.

[16] Y. Guo, H. Li and T. Zhai, *Advanced Materials*, 2017, **29**, 1–25.

[17] T. Krauskopf, F. H. Richter, W. G. Zeier and J. Janek, *Chemical Reviews*, 2020, **120**, 7745–7794.

[18] R. Chen, Q. Li, X. Yu, L. Chen and H. Li, *Chemical Reviews*, 2020, **120**, 6820–6877.

[19] Z. Zhang, Y. Shao, B. Lotsch, Y. S. Hu, H. Li, J. Janek, L. F. Nazar, C. W. Nan, J. Maier, M. Armand and L. Chen, *Energy and Environmental Science*, 2018, **11**, 1945–1976.

[20] Y. Zhao and L. L. Daemen, *Journal of the American Chemical Society*, 2012, **134**, 15042–15047.

[21] M. Dondelinger, J. Swanson, G. Nasymov, C. Jahnke, Q. Qiao, J. Wu, C. Widener, A. M. Numan-Al-Mobin and A. Smirnova, *Electrochimica Acta*, 2019, **306**, 498– 505.

[22] M.-H. Chen, A. Emly and A. Van der Ven, *Physical Review B*, 2015, **91**, 214306.

[23] X. Lü, J. W. Howard, A. Chen, J. Zhu, S. Li, G. Wu, P. Dowden, H. Xu, Y. Zhao and Q. Jia, *Advanced Science*, 2016, **3**, 1500359.

[24] A. K. Sagotra, D. Errandonea and C. Cazorla, *Nature Communications*, 2017, **8**, 963.

[25] R. Mouta, E. M. Diniz and C. W. Paschoal, *Journal of Materials Chemistry A*, 2016, **4**, 1586–1590.

[26] M. Wu, B. Xu, W. Luo, B. Sun and C. Ouyang, *Electrochimica Acta*, 2020, **334**, 135622.

[27] Y. Wang, H. Zhang, J. Zhu, X. Lü, S. Li, R. Zou and Y. Zhao, *Advanced Materials*, 2020, **32**, 1–17.

[28] C. Wang, K. Fu, S. P. Kammampata, D. W. McOwen, A. J. Samson, L. Zhang, G. T. Hitz, A. M. Nolan, E. D. Wachsman, Y. Mo, V. Thangadurai and L. Hu, *Chemical Reviews*, 2020, **120**, 4257–4300.

[29] E. Ahiavi, J. A. Dawson, U. Kudu, M. Courty, M. S. Islam, O. Clemens, C. Masquelier and T. Famprikis, *Journal of Power Sources*, 2020, **471**, 228489.

[30] A. Y. Song, Y. Xiao, K. Turcheniuk, P. Upadhya, A. Ramanujapuram, J. Benson, A. Magasinski, M. Olguin, L. Meda, O. Borodin and G. Yushin, *Advanced Energy Materials*, 2018, **8**, 1–11.

[31] J. A. Dawson, T. S. Attari, H. Chen, S. P. Emge, K. E. Johnston and M. S. Islam, *Energy and Environmental Science*, 2018, **11**, 2993–3002.

[32] Y. Li, W. Zhou, S. Xin, S. Li, J. Zhu, L. Xujie, Z. Cui, Q. Jia, J. Zhou, Y. Zhao and J. B. Goodenough, *Angewandte Chemie - International Edition*, 2016, **55**, 9965– 9968.

[33] Z. Lu, C. Chen, Z. M. Baiyee, X. Chen, C. Niu and F. Ciucci, *Physical Chemistry Chemical Physics*, 2015, **17**, 32547–32555.

[34] X. Lü, G. Wu, J. W. Howard, A. Chen, Y. Zhao, L. L. Daemen and Q. Jia, *Chemical Communications*, 2014, **50**, 11520–11522.

[35] I. Hanghofer, G. J. Redhammer, S. Rohde, I. Hanzu, A. Senyshyn, H. M. R. Wilkening and D. Rettenwander, *Chemistry of Materials*, 2018, **30**, 8134–8144.

[36] A. Koedtruad, M. A. Patino, N. Ichikawa, D. Kan and Y. Shimakawa, *Journal of Solid State Chemistry*, 2020, **286**, 121263.

[37] A. Song, K. Turcheniuk, J. Leisen, Y. Xiao, L. Meda, O. Borodin and G. Yushin, *Advanced Energy Materials*, 2020, **10**, 1903480.

[38] J. A. Dawson, P. Canepa, T. Famprikis, C. Masquelier and M. S. Islam, *Journal of the American Chemical Society*, 2018, **140**, 362–368.

[39] K. Shen, Y. Wang, J. Zhang, Y. Zong, G. Li, C. Zhao and H. Chen, *Physical Chemistry Chemical Physics*, 2020, **22**, 3030–3036.

[40] M. Wu, B. Xu, W. Luo, B. Sun, J. Shi and C. Ouyang, *Applied Surface Science*, 2020, **510**, 145394.

[41] A. Emly, E. Kioupakis and A. Van Der Ven, *Chemistry of Materials*, 2013, **25**, 4663– 4670.

[42] J. A. Dawson, H. Chen and M. S. Islam, *Journal of Physical Chemistry C*, 2018, **122**, 23978–23984.

[43] M. H. Braga, V. Stockhausen, J. C. Oliveira and J. A. Ferreira, *Materials Research Society Symposium Proceedings*, 2013, **1526**, 36–40.

[44] M. H. Braga, J. A. Ferreira, V. Stockhausen, J. E. Oliveira and A. El-Azab, *Journal of Materials Chemistry A*, 2014, **2**, 5470–5480.

[45] S. Stegmaier, J. Voss, K. Reuter and A. C. Luntz, *Chemistry of Materials*, 2017, **29**, 4330–4340.

[46] H. Fang and P. Jena, *ACS Applied Materials and Interfaces*, 2018, **11**, 963–972.

[47] H. Fang, S. Wang, J. Liu, Q. Sun and P. Jena, *Journal of Materials Chemistry A*, 2017, **5**, 13373–13381.

[48] H. H. Heenen, J. Voss, C. Scheurer, K. Reuter and A. C. Luntz, *Journal of Physical Chemistry Letters*, 2019, **10**, 2264–2269.

[49] P. Li, F. Hussain, P. Cui, Z. Li and J. Yang, *Physical Review Materials*, 2019, **3**, 115402.

[50] O. Reckeweg, B. Blaschkowski and T. Schleid, *Zeitschrift fur Anorganische und Allgemeine Chemie*, 2012, **638**, 2081–2086.

[51] A. Jones and M. S. Islam, *Journal of Physical Chemistry C*, 2008, **112**, 4455–4462.

[52] C. Tealdi, L. Malavasi, C. A. Fisher and M. S. Islam, *Journal of Physical Chemistry B*, 2006, **110**, 5395–5402.

[53] M. S. Islam, *Journal of Materials Chemistry*, 2000, **10**, 1027–1038.

[54] M. S. Islam and C. A. Fisher, *Chemical Society Reviews*, 2014, **43**, 185–204.

[55] M. S. Islam and R. A. Davies, *Journal of Materials Chemistry*, 2004, **14**, 86–93.

[56] R. Catlow, A. Sokol and A. Walsh, *Computational Approaches to Energy Materials*, John Wiley & Sons Ltd, Oxford, UK, 1st edn., 2013.

[57] M. Wu, B. Xu, X. Lei, K. Huang and C. Ouyang, *Journal of Materials Chemistry A*, 2018, **6**, 1150–1160.

[58] R. D. Shannon, *Acta Crystallographica Section A*, 1976, **32**, 751–767.

[59] J. A. Dawson, P. Canepa, M. J. Clarke, T. Famprikis, D. Ghosh and M. S. Islam, *Chemistry of Materials*, 2019, **31**, 5296–5304.

[60] Y. Deng, C. Eames, B. Fleutot, R. David, J. N. Chotard, E. Suard, C. Masquelier and M. S. Islam, *ACS Applied Materials and Interfaces*, 2017, **9**, 7050–7058.

[61] Y. Deng, C. Eames, L. H. Nguyen, O. Pecher, K. J. Griffith, M. Courty, B. Fleutot, J. N. Chotard, C. P. Grey, M. S. Islam and C. Masquelier, *Chemistry of Materials*, 2018, **30**, 2618–2630.

[62] A. R. Symington, J. Purton, J. Statham, M. Molinari, M. S. Islam and S. C. Parker, *Journal of Materials Chemistry A*, 2020, **8**, 19603–19611.

[63] B. G. Dick and A. W. Overhauser, *Physical Review*, 1958, **112**, 90–103.

[64] N. F. Mott and M. J. Littleton, *Transactions of the Faraday Society*, 1938, **34**, 485– 499.

[65] J. D. Gale and A. L. Rohl, *Molecular Simulation*, 2003, **29**, 291–341.

[66] S. Plimpton, *Journal of Computational Physics*, 1995, **117**, 1–19.

[67] D. J. Evans and B. L. Holian, *The Journal of Chemical Physics*, 1985, **83**, 4069– 4074.

[68] E. Wigner and F. Seitz, *Physical Review*, 1933, **43**, 804–810.

[69] A. Stukowski, *Modelling and Simulation in Materials Science and Engineering*, 2010, **18**, 015012.